occur at relatively lower temperatures. Di- and triiodides vaporize at around 1273 K during vacuum distillation but condense at different temperatures. The nonvolatile impurity oxyiodides remain in the Mo boat and can be separated from the diiodides completely. Thus, the oxyiodides do not affect the separation between di- and triiodides. We have conducted preliminary experiments on the separation of Sm and Dy at 1273 K from an iodide melt. The results calculated from the compositions of diiodide-rich and triiodide-rich deposits suggest a separation factor $\beta'_{Sm/Dy} = 2300$. The value is large enough to produce pure metals. Although thermodynamic properties of diiodides at elevated temperature have not been well established, the iodide route appears to be more promising for rare earth separation using the technique described here.

Wet processes such as solvent extraction are generally associated with complicated flow sheets (*1*). First, the rare earth raw minerals have to be decomposed and dissolved in aqueous solution. After an elaborate separation process for rare earths involving several cycles, concentration of the solution, precipitation, filtering, drying, and calcination are required for obtaining purified rare earth oxides. In the conventional reduction processes, the oxides are directly reduced to metals or converted to halides. The halides are then reduced to metals. Thus, the halides separated by the present process can be directly transferred to the conventional halide reduction process or used in the oxide reduction process after the pyrometallurgical conversion to oxides. The dry process proposed here provides an easier path with fewer process steps than the wet process. The differences in the redox potential and vapor pressure of compounds in different oxidation states of rare earths provide better opportunities for the design of suitable separation processes compared with the conventional process using only incremental variation of chemical properties with atomic number for a given oxidation state.

References and Notes

1. C. K. Gupta and N. Krishnamurthy, *Int. Mater. Rev.* **37**, 197 (1992).
2. K. L. Nash, in *Lanthanides/Actinides: Chemistry*, vol. 18 of *Handbook on the Physics and Chemistry of Rare Earths*, K. A. Gschneidner Jr. *et al.*, Eds. (Elsevier Science, Amsterdam, 1994), pp. 197–238.
3. J. Kaczmark, in *Industrial Applications of Rare Earth Elements*, K. A. Gschneidner Jr., Ed. (American Chemical Society, Washington, DC, 1981), pp. 135–166.
4. G. Adachi *et al.*, *J. Less Common Met.* **169**, L1 (1991).
5. K. Murase *et al.*, *J. Alloys Compounds* **198**, 31 (1993).
6. ———, *Bull. Chem. Soc. Jpn.* **65**, 2724 (1992).
7. D. A. Johnson, *Adv. Inorg. Chem. Radiochem.* **20**, 1 (1977).
8. G. Meyer, *Chem. Rev.* **88**, 93 (1988).
9. G. Czack *et al.*, *Gmelin Handbook of Inorganic Chemistry Sc, Y, La-Lu Rare Earth Elements Part C4b* (Springer-Verlag, Berlin, ed. 8, 1982).
10. I. Barin, *Thermodynamical Data of Pure Substances* (VCH, Weinheim, Germany, ed. 3, 1995).
11. L. S. Kudin *et al.*, *Electrochem. Soc. Proc.* **97-39**, 704 (1997).
12. A. V. Hariharan and H. A. Eick, *High Temp. Sci.* **4**, 91 (1972).
13. T. Uda, T. H. Okabe, Y. Waseda, K. T. Jacob, *J. Alloys Compounds* **284**, 282 (1999).
14. T. Uda, T. H. Okabe, Y. Waseda, *J. Jpn. Inst. Met.* **62**, 796 (1998).
15. G. I. Novikov and O. G. Polyachenok, *Russ. Chem. Rev.* **33**, 343 (1964).
16. D. A. Johnson, *J. Chem. Soc. A* **XX**, 2578 (1969).
17. G. Adachi, Ed., *Science of Rare Earths* (Kagakudojin, Kyoto, Japan, 1999), pp. 188–194.
18. J. Shibata and S. Matsumoto, *Mater. Sci. Forum* **315–317**, 268 (1999).
19. H. Bergmann, Ed., *Gmelin Handbook of Inorganic Chemistry Sc, Y, La-Lu Rare Earth Elements Part C6* (Springer-Verlag, Berlin, ed. 8, 1978).
20. L. R. Morss and T. G. Spence, *Z. Anorg. Allg. Chem.* **616**, 162 (1992).

21. We are grateful to T. H. Okabe and Y. Waseda of Tohoku University and K. Murase of Kyoto University for support and useful discussions.

20 June 2000; accepted 7 August 2000

A Mechanical Model for Intraplate Earthquakes: Application to the New Madrid Seismic Zone

Shelley J. Kenner*† and Paul Segall

We present a time-dependent model for the generation of repeated intraplate earthquakes that incorporates a weak lower crustal zone within an elastic lithosphere. Relaxation of this weak zone after tectonic perturbations transfers stress to the overlying crust, generating a sequence of earthquakes that continues until the zone fully relaxes. Simulations predict large (5 to 10 meters) slip events with recurrence intervals of 250 to 4000 years and cumulative offsets of about 100 meters, depending on material parameters and far-field stress magnitude. Most are consistent with earthquake magnitude, coseismic slip, recurrence intervals, cumulative offset, and surface deformation rates in the New Madrid Seismic Zone. Computed interseismic strain rates may not be detectable with available geodetic data, implying that low observed rates of strain accumulation cannot be used to rule out future damaging earthquakes.

During the winter of 1811 to 1812, three large intraplate earthquakes with cumulative magnitude $M_w = 7.5$ to 8.3 (*1*) occurred within the New Madrid Seismic Zone (NMSZ) (Fig. 1). Despite extensive research, our understanding of the processes that generate intraplate earthquakes such as these is limited. Seismicity in the NMSZ is presently limited to a zone ~250 km long (Fig. 1). Events on the two northeast trending lineaments have right-lateral mechanisms, whereas events in the northwest trending, compressional stepover are predominately reverse (*2*).

Dating of paleoliquefaction features and trenching along the central thrust fault reveal at least two prehistoric earthquakes of comparable size to the 1811–12 earthquakes, with interevent times of ~500 years (*3*). Fault slip during the 1811–12 earthquakes is estimated at ~8 m, based on isoseismal areas and empirical magnitude-length relations (*4*). Gravity and magnetic studies require strike-slip offsets of <10 km (*5*). However, dip-slip offsets of <70 to 80 m on the central thrust (*6*, *7*) limit cumulative strike-slip displacements to ~100 m, implying a recent initiation of faulting (*4*). Slip-rates on the central thrust fault increased from <0.001 mm/year before the Holocene to 1.8 mm/year during the Holocene and 6.2 mm/year in the Late Holocene (*7*).

Comparison of Global Positioning System (GPS) data with 1950s triangulation surveys indicated strain accumulation rates of 1.1×10^{-7} year^{-1} (0.44×10^{-7} to 2.0×10^{-7} at 95% confidence) in the NMSZ (*8*). GPS surveys conducted between 1991 and 1997, however, yield strain accumulation rates that are not significantly different from zero (*9*, *10*), given the current 95% confidence detection level of ~1×10^{-7} year^{-1} (*11*). GPS site velocities far from the seismic zone are negligible (*9*), consistent with the intraplate tectonic environment. The low strain-rates led Newman *et al.* to conclude that the potential for large earthquakes in the NMSZ was "significantly overestimated" (*9*). These authors interpret the geodetic velocities with an infinitely long screw dislocation (*12*) in

Department of Geophysics, Stanford University, Stanford, CA 94305, USA.

*To whom correspondence should be addressed. E-mail: kenner@gps.caltech.edu

†Present address: Division of Geological and Planetary Sciences, Seismological Laboratory, California Institute of Technology, Mail Code 252-21, Pasadena, CA 91125, USA.

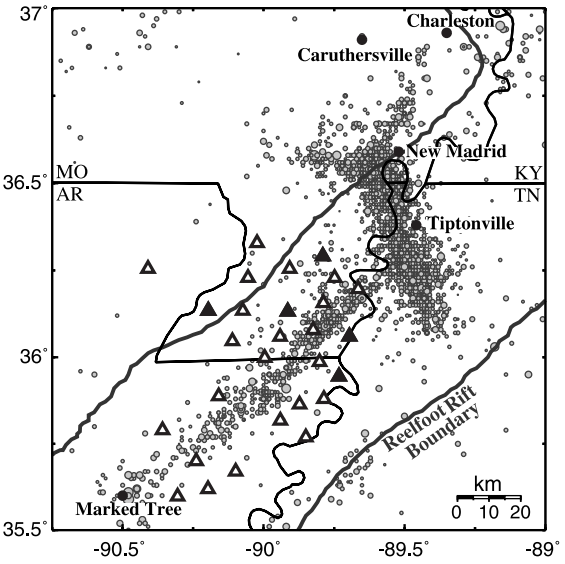

Fig. 1 (left). NMSZ in the south-central United States with seismicity shown by circles. Solid triangles denote sites in the continuous network used in the GPS uncertainty calculations. Solid and open triangles are included in the campaign network. All sites are part of the existing Stanford University campaign GPS network in the NMSZ.

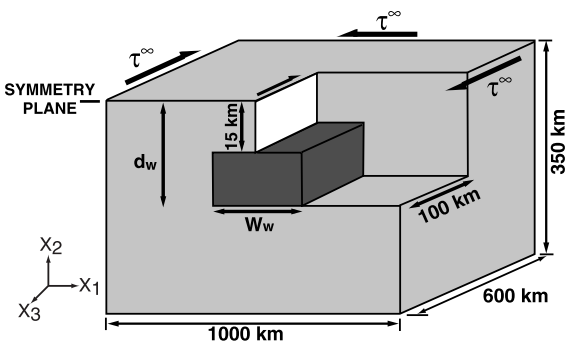

Fig. 2 (right). Model schematic. Light gray areas are elastic. Dark gray area is the weak zone. White area represents the seismogenic fault. W_w is the width and d_w is the depth to the base of the weak zone.

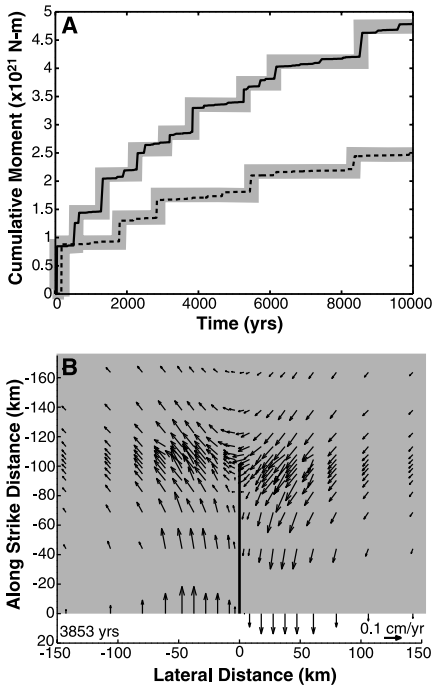

Fig. 3. (**A**) Cumulative moment versus time for (i) τ^{∞} = 60 MPa, τ^{max} = 62 MPa, and $\tau^{residual}$ = 50 MPa (thin solid line) and (ii) τ^{∞} = 25 MPa, τ^{max} = 27 MPa, and $\tau^{residual}$ = 15 MPa (thin dashed line). In both cases, W_w = 75 km and d_w = 40 km. Only the largest slip events are considered meaningful (thick gray lines). (**B**) Model 1 surface velocities immediately after a major earthquake at ~3850 years. The fault midpoint is at (0,0). The symmetry plane (*22*) is at x_3 = 0. For lower model stresses, e.g., Model 2, predicted surface velocities are lower by at least a factor of 2.

which relative far-field velocities equal the deep interseismic slip-rate, as appropriate for plate boundary settings. To properly interpret the geodetic data, we require a model appropriate for intraplate regions.

Table 1. Model rheologies and parameters. μ, the shear modulus, and ν, the Poisson's ratio, are applied uniformly. η_w is the weak zone viscosity.

Symbol	Magnitude range
η_w	10^{21} Pa-s
μ	35 GPa
ν	0.25
τ^{∞}	10 to 60 MPa
τ^{max}	12 to 75 MPa
$\tau^{residual}$	0 to 55 MPa
d_w	40 to 60 km
W_w	5 to 75 km

There is no widely agreed upon mechanical explanation for intraplate earthquakes (e.g., *13–16*). We present a time-dependent mechanical model for the generation of repeated large intraplate earthquakes. We explicitly include stress-controlled coseismic rupture and postseismic perturbations to the deformation field. As in the NMSZ, relative motions in the far field are zero (*9*).

The key to our model is a postulated lower crustal weak zone embedded within the elastic lithosphere. As in other intraplate seismic zones, the NMSZ is located within a repeatedly re-activated rift (*16–18*). Slightly elevated heat flow (*19*) and lower upper mantle velocities (*20*) suggest a locally weak lower crust and upper mantle (*15*, *21*). Relaxation of the weak zone could have been induced by a loss of strength due to, for example, a thermal or fluid pressure perturbation, or by a transient change in regional stress. Re-equilibration after such localized perturbations transfers stress to the upper crust. This may trigger slip on overlying faults, generating a sequence of earthquakes that continues until the weak zone reaches its fully relaxed state. Coseismic slip, in turn, partially reloads the lower crust causing cyclic stress transfer, which prolongs the relaxation process.

For weak zones of finite lateral extent subject to constant far-field stresses, the net fault offset remains finite as the weak zone relaxes. Consequently, the number of large slip events is finite. Thus, the model immediately satisfies observations of small cumulative fault offset, limited lateral extent of seismicity, and the absence of far-field relative motion. Finite element calculations (*22*) quantify the amount of coseismic slip, earthquake magnitudes, recurrence intervals, and surface deformation rates. The numerical model includes a three-dimensional rectangular weak zone (Fig. 2) with Maxwell viscoelastic rheology (*23*) and dimensions estimated from topographic, seismic (*20*), and gravimetric (*5*) investigations (Table 1). Initially, the entire body is uniformly stressed ($\tau_{13} = \tau^{\infty}$, all other components are zero) and in equilibrium with the far-field boundary conditions, τ^{∞}. In the calculations, an initially infinite weak zone viscosity is instantaneously decreased to some finite value. In reality, this loss of strength (e.g., thermal event) or a corresponding increase in stress would occur over a finite time interval. In each model earthquake, fault slip initiates when the resolved shear stress reaches τ^{max} at some point on the fault and continues until the stress is $\leq \tau^{residual}$ everywhere (*24*). Because slip weakening and dynamic rupture are not modeled, only general characteristics of the largest model slip events are resolved.

Estimates of τ^{∞} are obtained by requiring that the total fault offset u_{tot} does not exceed the observed bound of ~100 m (*6*, *7*). For an elastic crack $u_{tot} \approx 2(\tau^{\infty}/\mu)d_w$, if d_w = 40 km, τ^{∞} is ~44 MPa (*25*). If the upper mantle relaxes on a regional scale, the fundamental behavior of the model will not change but total fault displacement will scale with the length of the fault zone, allowing smaller stresses to drive equivalent slip. The charac-

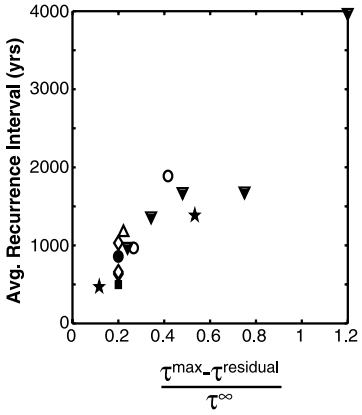

Fig. 4. Average $M > 7.5$ recurrence interval versus $(\tau^{max} - \tau^{residual})/\tau^{\infty}$ for all models during each 10,000 year simulation. Solid circle represents the reference model (Fig. 3A, Model 1). Diamonds give models with different W_w, squares different d_w, open circles different τ^{max}, open triangles different τ^{∞}, and stars different $\tau^{residual}$ with all other parameters as in the reference model. Solid triangles have a different τ^{∞}, but $(\tau^{max} - \tau^{residual})$ and $(\tau^{\infty} - \tau^{residual})$ are constant (e.g., Fig. 3A, Model 2).

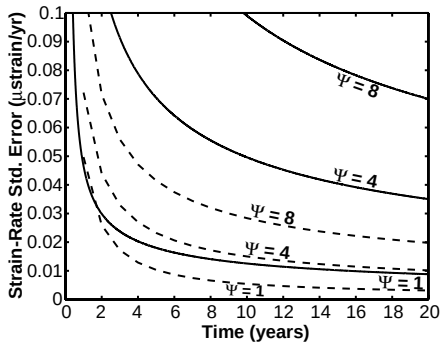

Fig. 5. Uncertainty (1σ) in engineering strain-rate versus time for two candidate networks (Fig. 1). Campaign measurements (dashed lines) are annual. Continuous measurements (solid lines) are recorded daily. Ψ (mm/$\sqrt{\text{year}}$) represents the scale of random walk processes associated with local benchmark motion. The greater number of stations in the campaign network more than compensates for the lower sampling rate, resulting in smaller uncertainties. Continuous stations, however, provide more information on temporally correlated noise sources.

teristic time for weak zone relaxation, which controls the duration of the earthquake sequence, is approximated by $T_{total} \approx 4.6(\eta_w/\mu)$ (*26*). For $T_{total} \approx 10{,}000$ years, we estimate a viscosity η_w of 10^{21} to 10^{22} Pa-s.

Numerical calculations show that relaxation of the weak zone generates a sequence of large slip events, with maximum offset of ~5 to 10 m and moment magnitudes of 7.5 to 8.0. Moment release rates decrease with time, and recurrence intervals, typically 250 to 4000 years, increase with time as the weak zone approaches its fully relaxed state and the earthquake generation process grinds to a halt (Fig. 3A). Reasonable variations in model parameters (Table 1) do not change this behavior. Increasing τ^{∞} increases the number of large events and the total offset, while decreasing the recurrence interval. A simple analytical model (*27*) suggests that recurrence interval scales with $(\eta_w/\mu)(\tau^{max} - \tau^{residual})/\tau^{\infty}$ and increases exponentially with $\mu t/\eta_w$. In fact, numerical estimates of average recurrence interval scale with the ratio $(\tau^{max} - \tau^{residual})/\tau^{\infty}$ (Fig. 4); however, they increase more slowly with time because of postseismic stress cycling.

Maximum interseismic fault parallel velocities occur at a lateral distance from the fault that depends on the weak zone's width and depth extent (Fig. 3B). At greater distances, velocities approach zero, as appropriate for intraplate regions. Velocities decay with time following the onset of relaxation ($t = 0$). For the considered parameters (Table 1), maximum velocities never exceed 1.5 cm/year. For more realistic models, in which the perturbation in weak zone strength or stress occurs over a finite time interval, peak velocities would be even lower. For relatively high remote stress (Fig. 3A, Model 1), engineering shear strain-rates, across a 100-km region bracketing the fault at its midpoint, immediately after large slip events at 1360, 3850 (Fig. 3B), and 8650 years, are ~1×10^{-7} year^{-1}, ~2×10^{-8} year^{-1}, and ~9×10^{-9} year^{-1}, respectively. For lower stress (Fig. 3A, Model 2), strain-rates are ~3.3×10^{-8} year^{-1}, ~1.8×10^{-8} year^{-1}, and ~5.5×10^{-9} year^{-1} at 1820, 2850, and 5500 years, respectively. For comparison, strain-rates along the San Andreas fault are ~3×10^{-7} year^{-1} to 6×10^{-7} year^{-1} (*28*). In our model, intraplate earthquakes are caused by stress transferred to the seismogenic fault from a local source in the lower crust and upper mantle. As a result, large earthquakes can occur every 500 to 1000 years, even though surface deformation rates are less than the detection level of prior GPS surveys, ~1×10^{-7} year^{-1} (*11*). This demonstrates that existing geodetic data cannot be used to rule out the occurrence of future damaging earthquakes in the NMSZ.

Model predictions of earthquake magnitude, coseismic slip, recurrence interval, cumulative offset, and surface deformation rate agree with observations from the NMSZ within uncertainties (*1*, *3–11*). Further work is needed to determine what might create a zone of weakness beneath the NMSZ (*15–21*) and to understand what processes acted in the Holocene to accelerate deformation. Local or regional perturbations in stress, pore pressure, or thermal state may have triggered weak zone relaxation. A strong candidate is recession of glacial ice sheets from central North America ~14,000 years ago (*29*, *30*) and subsequent sediment emplacement and subsidence in the Mississippi alluvial valley (*31*).

Though model-predicted strain-rates are low, they are detectable with well-designed geodetic experiments. The uncertainty in geodetic strain-rate depends on the number and distribution of stations, monument stability, the accuracy of the observations, and the observation interval. Assuming spatially uniform strain, random benchmark motions (*32*), and measurement error (*33*), we determine strain-rate uncertainty (*34*) for a 28-station campaign network and a 5-station permanent network (Fig. 1). The scale of the local benchmark wobble, characterized here as Gaussian random walk (*32*, *34*), ranges from <1 mm/$\sqrt{\text{year}}$ to as much as 4 mm/$\sqrt{\text{year}}$ in California (*32*); however, geodetic monuments in Mississippi valley sediments may be less stable. We find (Fig. 5) that strain-rate uncertainties of 1×10^{-8} year^{-1} can be achieved in 20 years with the 28-station network, as long as monument wander can be kept below 4 mm/$\sqrt{\text{year}}$. Uncertainties of the same magnitude can also be achieved with a smaller continuous network if monument wander is maintained at <1 mm/$\sqrt{\text{year}}$. Thus, predictions of the numerical models presented here can be tested within a reasonable time period, assuming careful attention is given to geodetic monument stability.

References and Notes

1. A. C. Johnston, *Geophys. J. Int.* **126**, 314 (1996); S. E. Hough, J. G. Armbruster, L. Seeber, J. F. Hough, *J. Geophys. Res.*, in press.
2. J. M. Chi, A. C. Johnston, Y. T. Yang, *Seismol. Res. Lett.* **63**, 375 (1992).
3. K. I. Kelson, G. D. Simpson, R. B. Van Arsdale, C. C. Haraden, W. R. Lettis, *J. Geophys. Res.* **101**, 6151 (1996); Y. Li, E. S. Schweig, M. T. Tuttle, M. A. Ellis, *Seismol. Res. Lett.* **69**, 270 (1998).
4. T. L. Pratt, *Seismol. Res. Lett.* **65**, 172 (1994); E. S. Schweig and M. A. Ellis, *Science* **264**, 1308 (1994).
5. T. G. Hildenbrand and J. D. Hendricks, in *Investigations of the New Madrid Seismic Zone*, K. M. Shedlock and A. C. Johnston, Eds., *U.S. Geol. Surv. Prof. Pap. 1538-E* (1995), pp. 1–30.
6. R. M. Hamilton and M. D. Zoback, in *Investigations of the New Madrid, Missouri, Earthquake Region*, F. A. McKeown and L. C. Pakiser, Eds., *U.S. Geol. Surv. Prof. Pap. 1236* (1982), pp. 55–82.
7. R. Van Arsdale, *Eng. Geol.* **55**, 219 (2000).
8. L. Liu, M. D. Zoback, P. Segall, *Science* **257**, 1666 (1992).
9. A. Newman *et al.*, *Science* **284**, 619 (1999).
10. S. Kerkela, M. H. Murray, L. Liu, M. D. Zoback, P. Segall, *Eos (Fall Suppl.)* **79**, 210 (1998).
11. The average maximum shear strain-rate within the campaign network (Fig. 1) is 0.003 ± 0.040 μrad/year. The uncertainty is scaled by 3.3 to account for misfit (possibly due to local site instabilities) of the station velocities to the spatially uniform strain assumption implicit in this calculation (M. H. Murray, personal communication).
12. J. C. Savage and R. O. Burford, *J. Geophys. Res.* **78**, 832 (1973).
13. W. J. Hinze, L. W. Braile, G. R. Keller, E. G. Lidiak, *Rev. Geophys.* **26**, 699 (1988).
14. J. Gomberg and M. Ellis, *J. Geophys. Res.* **99**, 20,299 (1994); J. P. Grana and R. M. Richardson, *J. Geophys. Res.* **101**, 5445 (1996); W. D. Stuart, T. G. Hildenbrand, R. W. Simpson, *J. Geophys. Res.* **102**, 27623 (1997).
15. L. Liu and M. D. Zoback, *Tectonics* **16**, 585 (1997).

16. L. W. Braile, W. J. Hinze, G. R. Keller, E. G. Lidiak, J. L. Sexton, *Tectonophysics* **131**, 1 (1986).
17. M. D. Zoback *et al.*, *Science* **209**, 971 (1980).
18. R. T. Cox and R. B. Van Arsdale, *Eng. Geol.* **46**, 210 (1997).
19. C. A. Swanberg and P. Morgan, in *Physical Properties of Rocks and Minerals*, Y. S. Touloukian, W. R. Judd, R. F. Roy, Eds. (McGraw-Hill, New York, 1981), vol. 2, pp. 540-548; C. A. Swanberg, B. J. Mitchell, R. L. Lohse, D. D. Blackwell, in *Investigations of the New Madrid, Missouri, Earthquake Region*, F. A. McKeown and L. C. Pakiser, Eds., *U.S. Geol. Surv. Prof. Pap. 1236* (1982), pp. 185–189.
20. A. Ginzburg, W. D. Mooney, A. W. Walter, W. J. Lutter, J. H. Healy, *Am. Assoc. Pet. Geol. Bull.* **67**, 2031 (1983); W. D. Mooney, M. C. Andrews, A. Ginzburg, D. A. Peters, R. M. Hamilton, *Tectonophysics* **94**, 327 (1983).
21. An alternative explanation for lower crustal weakness is proposed by M. F. Kane [in *Studies Related to the Charleston, South Carolina, Earthquake of 1886: A Preliminary Report*, D. W. Rankin, Ed., *U.S. Geol. Surv. Prof. Pap. 1028-O* (1977), pp. 199–204]. A weak crust is hypothesized to exist by (*5*), (*13*), (*18*), and F. A. McKeown and S. F. Diehl [in *Investigations of the New Madrid Seismic Zone*, K. M. Shedlock and A. C. Johnston, Eds., *U.S. Geol. Surv. Prof. Pap., 1538-N* (1994), pp. 1–24].
22. *ABAQUS User's Manual, version 5.8* [Hibbit, Karlsson & Sorensen, Inc., Pawtucket, RI (1998)]. Variably sized (minimum 0.2 km by 0.5 km by 0.25 km) brick elements are used. Variations in total number of elements (69%) and number of elements along the fault plane (53%) change the average recurrence interval for $M > 7.0$ events by ~100 years. A symmetry condition is applied along a plane oriented perpendicular to the fault at its midpoint (Fig. 2).
23. Maxwell viscoelastic materials have no long-term elastic stiffness. The weak zone could more reasonably be defined to have some long-term stiffness. Unless the stress relaxed by the weakening zone becomes too small to trigger fault slip, the fundamental behavior of the model would not change.
24. The shear stress failure criteria is evaluated at each node on the seismogenic fault plane (defined using contact surfaces) at each time increment. During any increment, nodes can fail either independently or in groups. For failure initiation, the maximum resolved stress must be within 1.6% of τ^{max} (time step is adjusted to meet this criteria). Multiple nodes cannot fail simultaneously unless the time step is ≤10 years. Variations in these criteria by a factor of 2 change the average recurrence interval for $M > 7.0$ events by ~50 years.
25. Stresses measured in deep boreholes [J. Townend and M. D. Zoback, *Geology* **28**, 399 (2000)] and shallow stress measurements from the NMSZ region [W. L. Ellis, in *Investigations of the New Madrid Seismic Zone*, K. M. Shedlock and A. C. Johnston, Eds., *U.S. Geol. Surv. Prof. Pap. 1538-B* (1994), pp. 1–13] are comparable.
26. For a Voigt solid with viscous element representing the lower crustal weak zone and elastic element representing the upper crust, the time for a fraction P of the total strain to accumulate following imposition of a fixed stress is $T_{total} = -\ln(1 - P)(\eta_w/\mu)$ where $P = 0.99$, $T_{total} = 10{,}000$ years, and $\mu = 3.5 \times 10^4$ MPa yields $\eta_w = 2.4 \times 10^{21}$ Pa-s. Because postseismic stress cycling between the upper and lower crust is not included in this approximation, numerical models require lower viscosities to obtain comparable characteristic relaxation times.
27. We estimate earthquake recurrence interval by the earthquake stress drop divided by the fault stressing rate. For a Maxwell layer of thickness h_2 underlying an elastic layer of thickness h_1, stressing rate is given by $\tau^{\infty}(h_2\mu/h\eta_w)\exp(-h_1\mu t/h\eta_w)$, where $h = (h_2 + h_1)$ (*35*) and t is time since the initiation of relaxation. The recurrence interval is given by $(\tau^{max} - \tau^{residual})/\tau^{\infty}(h\eta_w/h_2\mu)\exp(h_1\mu t/h\eta_w)$.
28. W. Thatcher, in *The San Andreas Fault System, California*, R. E. Wallace, Ed., *U.S. Geol. Surv. Prof. Pap. 1515* (1990), pp. 189–205.
29. T. J. Hughes *et al.*, in *The Last Great Ice Sheets*, G. H. Denton and T. J. Hughes, Eds. (Wiley, New York, 1981), pp. 275–318; P. A. Mayewski, G. H. Denton, T. J. Hughes, in *The Last Great Ice Sheets*, G. H. Denton and T. J. Hughes, Eds. (Wiley, New York, 1981), pp. 67–178; H. S. Hasegawa and P. W. Basham, in *Earthquakes at North Atlantic Passive Margins: Neotectonics and Postglacial Rebound*, S. Gregersen and P. W. Basham, Eds. (Kluwer, Boston, 1989), pp. 483–500; A. C. Johnston, in *Earthquakes at North Atlantic Passive Margins: Neotectonics and Postglacial Rebound*, S. Gregersen and P. W. Basham, Eds. (Kluwer, Boston, 1989), pp. 581–599.
30. B. Grollimund and M. D. Zoback [*Geology*, in preparation] suggest the possibility of glacial triggering in an anomalously weak NMSZ. Using a laterally homogeneous model, P. Wu and P. Johnston [*Geophys. Res. Lett.* **27**, 1323 (2000)] find that glacial triggering is unlikely.
31. R. T. Saucier, *Geomorphology and Quaternary Geologic History of the Lower Mississippi Valley* (U.S. Army Corps of Engineers, Mississippi River Commission, Vicksburg, MS, 1994), vol. 1, 362 pp., vol. 2, 28 plates.
32. J. Langbein and H. Johnson, *J. Geophys. Res.* **102**, 591 (1997).
33. We use an actual GPS covariance matrix from the NMSZ, representing the scaled weighted mean of daily solutions taken over a 2-week period in 1997. Horizontal uncertainties are ~3 mm.
34. We use a Kalman filtering approach following P. Segall and M. Matthews [*J. Geophys. Res.* **102**, 22391 (1997)] in which the data is assumed to result from a combination of uniform strain plus random benchmark motion and measurement error. We assume that the scale of the random walk process is known. Additional error would result if this parameter must be estimated directly from the data.
35. N. J. Kusznir and M. H. P. Bott, *Tectonophysics* **43**, 247 (1977).
36. We thank M. H. Murray for help with the GPS uncertainty analysis and B. Grollimund and M. D. Zoback for their insights regarding the NMSZ and glacial triggering.

25 May 2000; accepted 20 July 2000

Dating of Pore Waters with ^{129}I: Relevance for the Origin of Marine Gas Hydrates

Udo Fehn,[1]* Glen Snyder,[1] Per K. Egeberg[2]

Pore waters associated with gas hydrates at Blake Ridge in the Atlantic Ocean were dated by measuring their iodine-129/iodine ratios. Samples collected from sediments with ages between 1.8 and 6 million years ago consistently yield ages around 55 million years ago. These ages, together with the strong iodine enrichment observed in the pore waters, suggest that the origin of iodine is related to organic material of early Tertiary age, which probably is also the source of the methane in the gas hydrates at this location.

Gas hydrates are a potentially large source of energy and of greenhouse gases (*1*). Recent surveys suggest that they are ubiquitous features of continental slopes and that the energy equivalent of the methane in hydrates could potentially surpass that of all the known reservoirs of crude oil and natural gas combined. Marine gas hydrates commonly consist of methane trapped in a lattice of water ice (*2*) and are found in a specific depth range in marine sediments, typically between 200 and 500 m below the seafloor (mbsf). On seismic profiles, the bottom of the gas hydrate zone is indicated by a strong reflector, the bottom-simulating reflector (BSR). Below the BSR, free methane gas is common; its concentration is, however, considerably lower than the methane bound as gas hydrates.

The origin and formation of gas hydrates have been the focus of a growing number of studies (*1–3*). Although it is generally assumed that gas hydrates are related to the deposition and subsequent diagenesis of organic matter in marine sediments, no consensus exists on whether the methane in the hydrates formed at their present location or migrated from different source areas. To address this question, we used the ^{129}I system to date the origin of these hydrocarbons.

The cosmogenic radioisotope ^{129}I (half-life of 15.7 million years) is produced by the spallation of Xe isotopes in the atmosphere and by spontaneous fission of ^{238}U in the crust. Both of these mechanisms contribute similar amounts of natural ^{129}I to surface reservoirs (*4*). Iodine moves quickly through most surface reservoirs and is considered isotopically homogeneous at the surface of Earth, including the oceans and shallow sediments. The isotopic equilibrium of I in surface reservoirs has been disturbed recently by releases from weapons tests and reprocessing plants, which have increased the concentrations of ^{129}I in fresh waters, soils, surface ocean water, and shallow sediments by several orders of magnitude (*5–8*).

Iodine has one stable isotope, ^{127}I, and its isotopic composition is reported as $^{129}I/I$. Recent sediments without anthropogenic I have $^{129}I/I$ of 1.5×10^{-12} (*5*, *9*). This ratio, which is used as a starting value for ^{129}I-

[1]Department of Earth and Environmental Sciences, University of Rochester, Rochester, NY 14627, USA. [2]Department of Chemistry, Agder College, Tordenskjoldgate 65, 4604 Kristiansand, Norway.

*To whom correspondence should be addressed. E-mail: fehn@earth.rochester.edu